Journal of Materials Chemistry A

ROYAL SOCIETY OF CHEMISTRY

PAPER

View Article Online
View Journal | View Issue

Check for updates

Cite this: J. Mater. Chem. A, 2024, 12, 7711

Heterocycles for direct air capture and MOFs prepared from CO_2 utilization†

Jingcheng Du,[a] Linghao Liu,[a] Qian Sun,[a] Ziye Song,[a] Ayan Yao,[a] Ji Ma,[a] Tai-Shung Chung, *[bc] Wei Xu,[d] Hongjun Zhang [d] and Jiangtao Liu *[a]

Received 14th November 2023
Accepted 13th February 2024

DOI: 10.1039/d3ta07024g

rsc.li/materials-a

The technology for carbon capture, utilization, and storage (CCUS) has drawn global attention because of the rapid climate changes. Herein, a series of nitrogen-rich heterocycles (HC_x–N_y) was identified for direct air capture (DAC) based on a phase change mechanism. HC_x–N_y possessed a CO_2 removal efficiency of up to 99% under continuous CO_2 flow with a concentration of 437 ppm *via* spontaneous CO_2 fixation because it has a high CO_2 sorption capacity of 23.82 mol kg^{-1}. Based on this phenomenon, a green and highly efficient strategy was discovered to utilize CO_2 for different MOF syntheses *via* altering monomers and anions (SO_4^{2-}, OAC^-, and NO_3^-). Furthermore, we made a novel discovery that anions significantly affect the topological structures and morphologies of MOFs. Hence, from the discovery of nitrogen-rich heterocycles (HC_x–N_y) to direct air carbon capture to the synthesis of high value-added MOFs and then to the construction of high-performance gas separation membranes, this integrated strategy provided significant insights into the development of a comprehensive CCUS technology.

Introduction

Carbon dioxide is the main contributor to the global greenhouse effect, and its atmospheric levels are increasing through human activities such as anthropogenic emissions into the atmosphere from fossil-fuel-based power plants, cement and steel industries, and automobiles. Thus, the global temperature has risen, and climate catastrophe has been triggered in recent decades, posing a threat to the living systems.[1–3] According to an authoritative data analysis,[4] the average decadal growth rates of global carbon emissions were 2.8%, 1.3%, 1.1%, 2.7% and 1.7% for each decade since the 1970s. Global annual emissions increased from 33.3 $GtCO_2$ in 2020 to 34.9 $GtCO_2$ in 2021, representing a 4.8% increase. Therefore, it is urgent to reduce CO_2 emissions and establish a carbon-neutral society.[5] In order to deal with the global CO_2 challenge, countries around the world have made commitments to reduce greenhouse gas emissions according to the Paris Agreement:[6] (1) the European Union would reduce 40% greenhouse gas emissions by 2030 compared to the base year of 1990, (2) the United States would reduce 26–28% by 2025 compared to the base year of 2005, (3) Australia and Canada would reduce 26–28% and 30%, respectively, by 2030, and (4) China would achieve the carbon peak by 2030 and carbon neutrality by 2060.

Hence, breakthroughs in innovative carbon capture, utilization, and storage (CCUS) must be advanced. Traditionally, carbon capture can be implemented based on three main technologies, including pre-combustion carbon capture, post-combustion carbon capture, and oxy-combustion.[7] However, these techniques require stationary CO_2 sources, such as large industrial processes and power plants. Generally, it is easy to capture CO_2 from the flue gas of these plants because of high CO_2 concentrations. In contrast, it is extremely challenging to capture CO_2 from dispersed and mobile sources with low CO_2 concentrations of ~400 ppm, which is a typical CO_2 concentration in the atmosphere. Therefore, developing an advanced technology that can extract CO_2 from ambient air has become necessary and urgent. Such technology has been referred to as "direct air capture" (DAC), first introduced by Lackner *et al.* in 1999.[8] So far, the trade-off relationship between efficiency and capacity in DAC has hindered its further development for practical applications. The ideal materials to mitigate greenhouse gases directly from the atmosphere must satisfy the following characteristics (1) operatable at room temperature and near ambient conditions, (2) effective in all humidity conditions to maintain high CO_2 capture performance.

Currently, many technologies to capture CO_2 have been developed, such as energy-saving gas separation membranes,[9] eco-friendly CO_2 adsorbents,[10,11] and high-efficiency photocatalytic or electrocatalytic reduction.[12] Although these

[a]Department of Environmental Science and Engineering, University of Science and Technology of China, Hefei, 230052, China. E-mail: jiangtaoliu@ustc.edu.cn
[b]Department of Chemical and Biomolecular Engineering, National University of Singapore, 117576, Singapore. E-mail: chencts@nus.edu.sg
[c]Graduate Institute of Applied Science and Technology, National Taiwan University of Science and Technology, Taipei 10607, Taiwan
[d]State Key Laboratory of Particle Detection and Electronics, University of Science and Technology of China, Hefei, 230052, China

† Electronic supplementary information (ESI) available. See DOI: https://doi.org/10.1039/d3ta07024g

approaches can effectively capture CO_2, they have disadvantages. Membrane separation technology has a trade-off relationship between CO_2 permeability and selectivity, which is always the bottleneck impeding the development of advanced membranes. Adsorption technology makes it difficult to regenerate CO_2, which is often accompanied by high energy consumption. Photoelectric catalysis has the disadvantages of requiring special equipment, instability of catalysts, unique reaction conditions and inadequate reaction efficiency, which makes it difficult for large-scale practical applications. In addition to overcoming the above bottlenecks and capturing CO_2 at high efficiency, the practical applications of CCUS must utilize the captured CO_2 as a starting material for high value-added products. Literature research has indicated that high value-added substances, such as organic carbonates,[13] chemoenzymatic starch,[14] and long-chain compounds (glucose and fatty acids),[15] have been unbelievably synthesized by utilizing CO_2 as the raw material, which are the milestones of great significance to advance R&D for CCUS. The syntheses of the above products inevitably involved lengthy processes, special catalysts, and complicated reaction conditions due to the inert nature of CO_2. Up to now, the preparation of high value-added MOFs using CO_2 as the starting material in mild conditions is still very difficult and rarely reported.

MOFs, composed of metal clusters with polydentate ($\geq$2) organic ligands containing O, N or P groups, are usually made by the self-assembly of coordination bonds under certain conditions to form 0D, 1D, 2D, or 3D porous skeleton materials, which are one of the most advanced porous crystal materials in the 21st century.[16,17] Compared with traditional porous materials (zeolite and activated carbon), MOFs have numerous merits, such as variable secondary building units (SBUs), adjustable length and functional ligand, controllable pore size and high specific surface area varying from 1000 to $\sim$10 000 m^2 g^{-1}.[18] They have been widely used in gas adsorption,[19] separation,[20] sensing,[21] catalysis[22] and other fields.[23] Inspired by these merits and a broad range of applications, a variety of strategies have been designed to prepare MOFs, including solvothermal synthesis,[24] microwave synthesis,[25] ultrasonic synthesis[26] and other synthetic approaches.[27] Nevertheless, most of the methods have the shortcomings of high energy consumption, long reaction time, low yield, and the demand for harmful solvents and specific equipment, which violates the principle of low energy consumption, green sustainable development and large-scale production. Adaptation to the above criteria is necessary for the sustainable development of human society and the large-scale preparation of MOFs.

To achieve the double objectives of discovering superior materials for high-efficiency DAC from air and constructing high-value MOFs from the captured CO_2 for gas separation, high geometric symmetry and various sizes of heterocycle HC_x–N_y with different nitrogen-rich contents (*i.e.*, as capture sites) were selected for preliminary investigation in this study where "H" stands for heterocycle, "C_x" and "N_y" stand for the numbers of carbon atoms and nitrogen atoms in the heterocycle, respectively. Our preliminary results have indicated that HC_x–N_y are promising materials for DAC because they have extremely high absorption rates and capacities with unprecedented states *via* the phase change process. In addition, benefiting from their high activity and symmetry of geometry, HC_x–N_y was further selected as precursors for the CO_2-derived linkers because they were able to react with two, three or four CO_2 molecules to produce the di-carbamate, tri-carbamate and tetra-carbamate salts of $[HC_4–N_2–CO_2]^{2-}$, $[HC_6–N_3–CO_2]^{3-}$ and $[HC_{10}–N_4–CO_2]^{4-}$ under room temperature and pressure without any catalyst.[28] As $[HC_4–N_2–CO_2]^{2-}$, $[HC_6–N_3–CO_2]^{3-}$ and $[HC_{10}–N_4–CO_2]^{4-}$ have two, three and four coordination sites located at six-, nine-, and fourteen-membered rings that own polydentate ligands, and they also define the bridging orientation of the metal clusters. Based on the coordination design criteria of MOFs, it is extremely crucial to select polydentate ligands and metal clusters for perfect porous crystal frameworks. Considering the conditions for ligand preparation and the formation environment for MOFs, a zinc salt was selected to form metal clusters at room temperature. To the best of our knowledge, in the literature, the reactions of HC_6–N_3 and HC_{10}–N_4 with CO_2 or with metal clusters to form MOFs have not been reported. Furthermore, for the first time, we were able to use the CO_2-derived ligands to coordinate with the same metal clusters but different anions (SO_4^{2-}, NO_3^-, and OAC^-) to synthesize MOFs of diverse morphologies. In order to explore the superiority of nitrogen-rich MOFs, the obtained MOFs were introduced into PIM-1 to optimize the pore characteristics (such as reducing micropore sizes and narrowing PSD) of membranes to construct CO_2 channels and significantly enhance the separation performance. Introducing our new MOFs in MMMs may synergistically break the permeability selectivity trade-off limit and surpass the conventional upper bound.

Results and discussion

Visible DAC capacity

Visible proof of HC_x–N_y for DAC at an ultralow CO_2 concentration is extremely important (Fig. 1). To investigate its capture performance, various other advanced materials were also examined and compared by studying their CO_2 absorbing capacities from (1) the CO_2 exhaled by a human body with a maximum CO_2 concentration of 2–5% and (2) the atmosphere containing 408 ppm CO_2 (Fig. S1†). As exhibited in Fig. S2a, b and Video S1,† once the exhaled CO_2 was in contact with HC_4–N_2 or HC_6–N_3 molecules, white precipitates HC_4–N_2–CO_2 or HC_6–N_3–CO_2 were formed immediately with an absorption duration of <5 s for HC_6–N_3, showing a high affinity and excellent absorption rate toward CO_2. This characteristic is essential for a material suitable for DAC. In contrast, experimental difficulties were significantly increased by using HC_6–N_3 in the air capture equipment to capture CO_2 in the atmosphere (Fig. S2c†). However, by injecting air into the HC_6–N_3 solution, a small amount of white precipitate was also generated, indicating successful CO_2 capture at an ultralow concentration, as demonstrated in Fig. S2d.† Analyses by field emission scanning electron microscopy (FESEM) indicated that the microscopic morphology of the white precipitate was circular vesicles, with size in the range of 0.2–1.2 nm (Fig. S3†). For quantitative

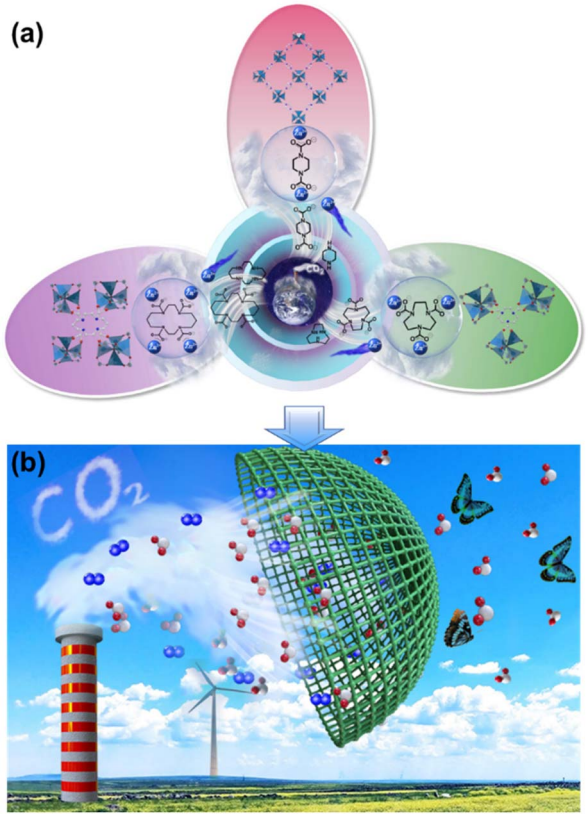

Fig. 1 Schematic diagram of synthetic MOFs and membrane separation. (a) Schematic diagram of the process for MOF synthesis from Zn clusters and various nitrogen-rich heterocycles by introducing CO_2 at room temperature and atmospheric pressure *via* a one-pot method. (b) Membrane separation diagram for CO_2/N_2 separation.

analyses of the removal efficiency under ultralow CO_2 concentrations, a CO_2 testing system was set up, including an air source, absorption reactor and detection system, as shown in Fig. S2e and S4.† An air source comprising 437 ppm CO_2 was injected into the homogeneous reaction system consisting of HC_x–N_y and acetonitrile (MeCN). After the DAC process, the downstream gas entered a nondispersive infrared meter to analyze the CO_2 concentration. HC_4–N_2 showed the best removal efficiency of more than 90% from the ultralow CO_2 stream within 12 hours because its electron-rich characteristics facilitated the reaction with CO_2. Thus, it has far better CO_2 capture capability than conventional CO_2 absorbers (MEA and KOH). (Fig. S1f, S5 and Video S2†). These results are quite encouraging because the newly discovered HC_x–N_y materials display the superior capability to reduce the CO_2 concentration in the atmosphere, and a carbon-neutral society can therefore be potentially achieved in the near future.

Table S1† summarizes a comparison of CO_2 absorption capacity between HC_x–N_y and other high-performance adsorbents, such as MOFs, zeolites, ionic liquids, amine-decorated mesoporous solids, aza-fused π-conjugated networks and amine solution adsorbents reported in the state-of-the-art literature. The CO_2 absorption capacities of HC_x–N_y are 2 to 8 times higher than those of MEA, MOFs, and bipy-CTF500. To the best of our knowledge, it is one of the best materials in terms of CO_2 absorption capacity.

Fabrication of HC_x–N_y–CO_2(–Zn)

In addition to the discovery of HC_x–N_y for DAC, the preparation of MOFs from CO_2 is also a focus of this work. The synthetic process of MOFs is shown in Fig. 1a. The HC_x–N_y–CO_2–Zn MOFs powders were prepared by means of *in situ* synthesis *via* a one-pot approach utilizing CO_2 at 25 °C. Introducing CO_2 into a mixed solution of $Zn(OAc)_2 \cdot 2H_2O$, HC_x–N_y in *N*,*N*-dimethylformamide (DMF) and 2-propanol (IPA) or MeCN led to the formation of a white product at different reaction durations in a homemade device (Fig. S6†). Although HC_x–N_y emerged to be highly symmetrical and similar structures, discrepancies in their ring sizes led to slightly different reaction times and conditions for better crystal growth (Fig. S7–S9†). Distinguishing from the one-step syntheses of HC_4–N_2–CO_2–Zn and HC_6–N_3–CO_2–Zn, HC_{10}–N_4–CO_2–Zn was prepared by first synthesizing HC_{10}–N_4–CO_2 and then further dissolved in an IPA solvent and reacted with Zn^{2+} for a period of time to obtain crystal MOFs at 80 °C (Fig. S9†).

Afterwards, the MOFs would be used to prepare the membrane for gas separation (Fig. 1b).

Characterizations of HC_x–N_y–CO_2(–Zn)

Based on Fig. 2a, d and g, the configurations of ball-and-stick models of HC_4–N_2–CO_2, HC_6–N_3–CO_2 and HC_{10}–N_4–CO_2 in the lowest energy states indicate that the noncoplanar carbon atoms are able to wiggle, which endows the frameworks with flexibility. The flexible HC_4–N_2–CO_2 ligands can construct flexible MOFs by reacting with SBUs. Flexible MOFs represent a particular subgroup within the class of hybrid materials, namely, the third-generation compounds or soft porous crystals.[29] Compared with conventional MOFs, flexible MOFs have been widely used to construct stimulus-responsive MOFs due to their excellent attributes of variable structures, such as unique responses from guest molecules, light, temperature, electrical fields, and pressure. Therefore, MOFs with excellent properties possess broad prospects as smart materials.

Before synthesizing MOFs, the reactions between HC_4–N_2, HC_6–N_3, HC_{10}–N_4 and CO_2 were firstly conducted at room temperature and the morphologies of the resultant ligands (*i.e.*, HC_4–N_2–CO_2, HC_6–N_3–CO_2 and HC_{10}–N_4–CO_2) were examined and compared. As illustrated in Fig. 3, the variational morphologies of HC_x–N_y–CO_2 arise from different ring sizes and numbers of the secondary amine groups in HC_x–N_y. HC_4–N_2–CO_2 exhibits an evenly distributed and regular ribbon-like morphology with a width of ~1 μm (Fig. 2b and c). In contrast, HC_6–N_3 is so deliquescent in air that it is difficult to obtain its microscopic morphology under FESEM. However, the resultant HC_6–N_3–CO_2 shows excellent stability in air and has an intriguing lychee-like morphology accompanied by some small bumps on the surface, which have a radius of ~4 μm (Fig. 2e and f). Besides, HC_{10}–N_4 has an interesting needle-like morphology at the macro scale (Fig. S10a†). Under FESEM, HC_{10}–N_4 appears to have a rod shape of ~200 μm length and

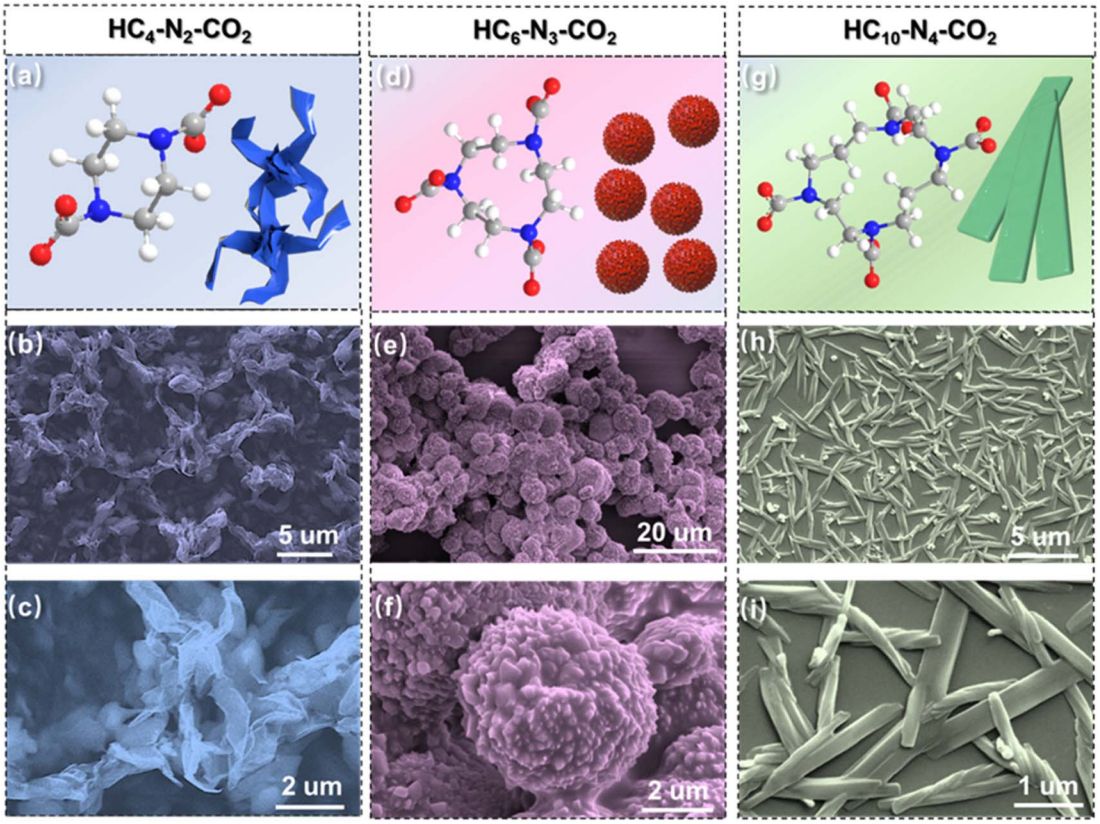

Fig. 2 Molecular structure and morphology of HC_x–N_y–CO_2: (a–c) HC_4–N_2–CO_2, (d–f) HC_6–N_3–CO_2, and (g–i) HC_{10}–N_4–CO_2. All the ball and stick model states of HC_x–N_y–CO_2 are in the lowest energy states optimized through Chemdraw 3D. Different colored spheres represent different atoms, where blue is N, gray is C, and red is O.

~20 μm width (Fig. S10b–S10e†). After the CO_2 reaction, the lamellar HC_{10}–N_4–CO_2 is obtained with an average length of ~3 μm and width of ~400 nm (Fig. 2h and i). To our knowledge, the fantastic ribbon-like HC_4–N_2–CO_2, lychee-like HC_6–N_3–CO_2, and lamellar-like HC_{10}–N_4–CO_2 have been prepared successfully for the first time at room temperature. These intriguing ligands would further react with metal clusters to form MOFs by coordination bonds.

Formation mechanism of HC_x–N_y–CO_2

Considering the interesting morphological changes from HC_x–N_y to HC_x–N_y–CO_2, a possible mechanism is proposed based on our experimental results and the previous literature.[30,31] As manifested in Fig. 3a, the reactions in this system can be divided into three main stages based on the phase change mechanism, in which a liquid HC_x–N_y has been changed into a solid HC_x–N_y–CO_2 based on the reaction of [$R^1R^2NH(l)$ + $CO_2(g)$ → R^1R^2N–$COOH(s)$]. The underlying mechanism of this reaction can be described as follows: The electrophilic nature of the C atom in CO_2 makes it susceptible to being attacked by nucleophilic N from HC_x–N_y. The secondary amines can act as nucleophiles by directly attacking the free CO_2 to form a zwitterion, which rapidly rearranges into carbamic acid *via* intramolecular proton transfer. The carbamic acid may be converted into a carbamate by transferring the proton to another free amine (*i.e.*, a Brønsted base). Primarily, a homogeneous phase system is established by dissolving HC_x–N_y as a strong Lewis base in organic solvents to provide sufficient active sites to electrophilic CO_2 at the molecular level. In the second stage, the electron-rich secondary amine of HC_x–N_y (*i.e.*, strong nucleophile) reacts quickly with CO_2 molecules to form the monocarbamate (*i.e.*, the formation of a heterogeneous phase). The reaction is rapid within a few seconds because the strong nucleophile attack of HC_x–N_y and the formation of a solid phase promote the reaction in a forward direction. In the third stage, more CO_2 is reacted with mono-carbamate to form di-carbamate, tri-carbamate or tetra-carbamate (*i.e.*, the formation of a more heterogeneous phase). This stage is the rate-determining step due to the complex environments of CO_2 reaction, steric hindrance and changes in the electronic structure.[35] As an example, Fig. S11† exhibits the digital pictures of the reaction process between HC_6–N_3 and CO_2 at different durations of 0 s, 5 s and 2 h, demonstrating an extremely high reactivity.

Experimentally, the viscosity of the reaction system increased when the reaction proceeded, which further confirmed the reaction progress as more heterogeneous phases were formed. The viscosity result was consistent with the above model mechanism. Specifically, the two nucleophilic secondary amine bonds of HC_4–N_2 reacted quickly with two electrophilic

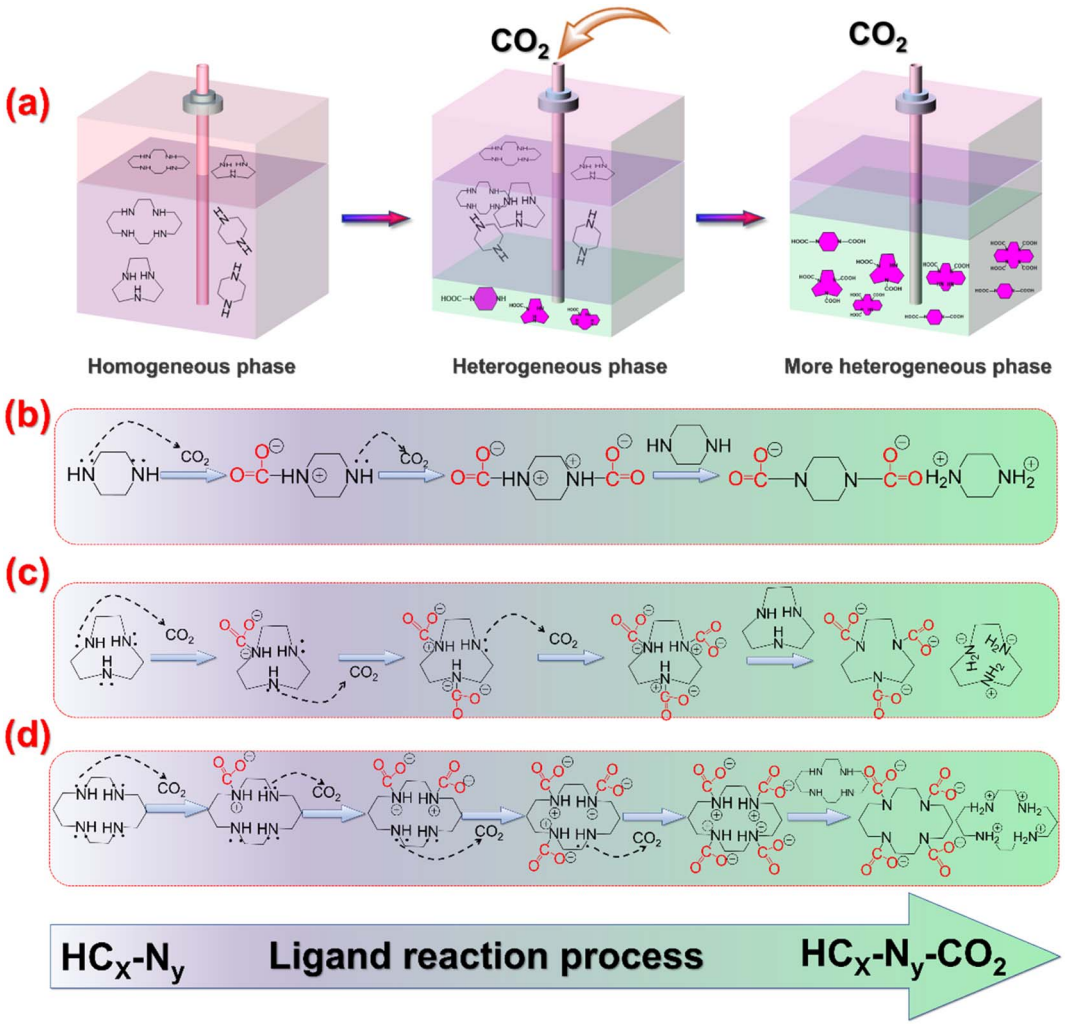

Fig. 3 Formation mechanism of HC_x–N_y–CO_2. (a) Model process diagram to form HC_x–N_y–CO_2 including mainly three stages (homogeneous phase, heterogeneous phase, and more heterogeneous phase). Mechanisms of ligand formation for MOFs between electrophilic CO_2 and nucleophilic starting materials. (b) HC_4–N_2. (c) HC_6–N_3. (d) HC_{10}–N_4.

CO_2 molecules to form solid di-carbamate (Fig. 3b). Due to the high activity of the secondary amine bonds, the di-carbamate yield was up to 99.96%, according to the quantitative analysis of a liquid nuclear magnetic hydrogen spectrum (Fig. 6f). Following a similar mechanism, electron-rich HC_6–N_3 or HC_{10}–N_4 reacted with three or four CO_2 molecules, respectively, to form tri-carbamate or tetra-carbamate (Fig. 3c and d). In addition, as depicted in Table S2,† HC_x–N_y has a very high nitrogen content; for instance, 1 equivalent HC_4–N_2, HC_6–N_3, and HC_{10}–N_4 have 0.326, 0.326, and 0.28 equivalent N atoms, respectively. These N contents, as active sites, are higher than those of all advanced CO_2 adsorbents at present, which plays an important role in the adsorption of CO_2 with a high speed and capacity. Moreover, according to theoretical calculations, 1 equivalent HC_4–N_2 absorbs 1.048 equivalent CO_2, 1 equivalent HC_6–N_3 absorbs 1.0476 equivalent CO_2, and 1 equivalent HC_{10}–N_4 absorbs 0.898 equivalent CO_2. However, with the increase in secondary amine bonds, the steric hindrance of the subsequent reaction becomes greater, leading to difficulties in completing the reaction, which would be confirmed in the subsequent experiments. After the flexible ligands are obtained, these HC_x–N_y–CO_2 ligands can be further reversibly deprotonated and coordinated with zinc clusters to synthesize MOFs with different void sizes.

Formation process of the hollow flower-like HC_4–N_2–CO_2–$ZnSO_4$

Inspired by the innovative syntheses of MOF-5,[32] MOF-38($Zn_3(btc)_2$)[33] and Zn_2(TPOM)$(btc)_2$ (ref. 34) made of terephthalic acid (1,4-H_2bdc), trimesic acid (1,3,5-H_3btc), benzene-1,2,4,5-tetracarboxylic acid (1,2,4,5-H_4btc) and Zn clusters, HC_4–N_2–CO_2, HC_6–N_3–CO_2 and HC_{10}–N_4–CO_2 ligands were used to form MOFs with zinc clusters. In terms of HC_4–N_2–CO_2–$ZnSO_4$, a charming micron flowery sphere (like hydrangea) with a diameter of ~3 μm was prepared by *in situ* synthesis of HC_4–N_2 and $ZnSO_4$ with CO_2 involved *via* self-assembly of the nanosheets with a thickness of ~100 nm (Fig. 4b–d and S12†). Ultimately, field emission transmission electron microscopy

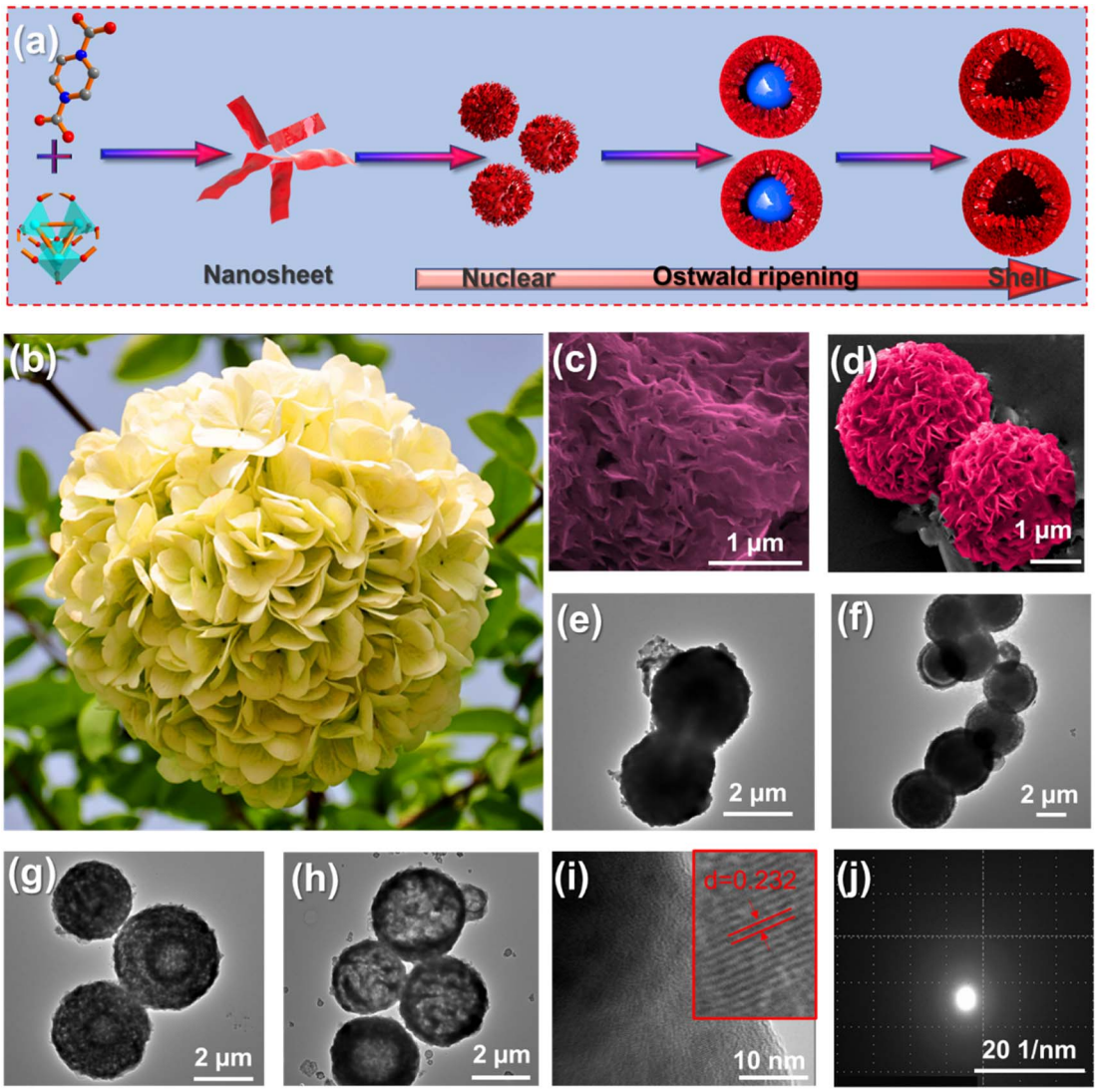

Fig. 4 Formation process of hollow flower-like HC_4–N_2–CO_2–$ZnSO_4$. (a) Model diagram of hollow flower formation according to an inside-out Ostwald ripening process. (b) A digital picture of hydrangea. (c and d) FESEM images. FESEM images were colored red for visual effect. (e–h) Low-magnification TEM images. (i) HR-FETEM image. (j) SAED pattern of HC_4–N_2–CO_2–$ZnSO_4$.

(FETEM) undoubtedly corroborated that HC_4–N_2–CO_2–$ZnSO_4$ had a hollow-shell structure (Fig. 4h). The interesting morphology might result from an inside-out Ostwald ripening process.[35,36] As illustrated in Fig. 4a, the formation processes of the hollow flower-like structure mainly included the following four stages: (I) lamellar HC_4–N_2–CO_2–$ZnSO_4$ was formed through the reaction among CO_2, HC_4–N_2 and $ZnSO_4$ (Fig. 4c). (II) The lamellar HC_4–N_2–CO_2–$ZnSO_4$ self-assembled into dense inner nuclear MOFs (Fig. 4e), but the high surface energy of the inner nuclear led to instability owing to the mismatch defects generated during the initial fast growth process and the higher curvature of the spheres with a smaller radius. (III) The intermediate core–shell structure was formed from dense MOFs to hollow flower-like MOFs in order to reduce the high surface energy. According to Fig. 4f, some small cavities appeared between the core and shell. As MOFs continued to grow, the small cavity gradually became larger, as shown in Fig. 4g. (IV) Inner crystallites of HC_4–N_2–CO_2–$ZnSO_4$ migrated from the inner core and self-assembled at the outer walls of the hollow flower to minimize the surface energy of the system. The morphological change was from a small inner core (Fig. 4g) to a hollow flower (Fig. 4h). The high-resolution FETEM (HR-FETEM) image presented lattice fringes of HC_4–N_2–CO_2–$ZnSO_4$ (Fig. 4i), and a SAED pattern was obtained (Fig. 4j). These analyses revealed that a crystal consisting of hollow flower-like MOFs was acquired successfully.

The existence of interior space in the shell of HC_4–N_2–CO_2–$ZnSO_4$ particles verifies their unique characteristics, such as confined reaction and low mass transfer resistance, which are essential for subsequent applications, such as catalyzed synthesis,[37] sodium-ion batteries,[38] and photoelectron catalytic conversion.[39] So far, most hollow-shell structure materials must be prepared at high temperatures or by introducing an appropriate template, which is extremely difficult and rare to synthesize

at room temperature. Therefore, utilizing CO_2 to prepare MOFs particles with hollow flower-like structures through a simple room temperature strategy appears more innovative and conducive to CO_2 conversion and environmental protection.

Effect of anions (OAC^-, SO_4^{2-}, NO_3^-) on MOFs formation

To the best of our knowledge, most research on MOFs has mainly focused on the influence of different types of SBUs[40] and ligands,[41] but has not explored the influence of anions on MOFs formation. Therefore, the same Zn clusters were employed as the metal source with similar synthesis conditions, but dissimilar anions were used to explore their effects on morphology. By substituting sulfate (SO_4^{2-}) with acetate (OAC^-), a high aspect ratio laminar HC_4–N_2–CO_2–$Zn(OAC)_2$ was obtained, which had an even size of ~2.5 μm length, ~400 nm width and ~80 nm thickness (Fig. 5f and f1). A further modification of anions by nitrate (NO_3^-) resulted in HC_4–N_2–CO_2–$Zn(NO_3)_2$ with an entirely different morphology of tremellar shape *via* the bending and folding of a large layer of ~10 nm thickness (Fig. 5g and g1). The above results illustrate that the introduction of distinct anions (SO_4^{2-}, OAC^-, NO_3^-) has a significant effect on MOFs morphology because anions can change the topological type of MOFs due to the template mechanism of anions.[42–44] Anions (SO_4^{2-}, OAC^-, NO_3^-) as templating agents are used to link together different organic and metal-containing building blocks into assemblies with high selectivity for the templating anions. Meanwhile, due to the differences in the coordination of different anions with metal-containing building blocks, MOFs with different topological configurations were obtained. This phenomenon has rarely been reported in the literature.[45]

To further elucidate the universality of different anions (SO_4^{2-}, OAC^-, NO_3^-) resulting in dissimilar MOFs morphologies, HC_6–N_3–CO_2–Zn and HC_{10}–N_4–CO_2–Zn were also prepared from the same Zn clusters with different anions (NO_3^-, OAC^-). Firstly, the influence of OAC^- and NO_3^- anions on the formation of MOFs prepared from HC_6–N_3, CO_2 and Zn clusters was studied *via* a similar approach. According to Fig. 5h and h1, the blocky-like HC_6–N_3–CO_2–$Zn(OAC)_2$, which had a proportion of ~2 μm length and ~1 μm width, was obtained in the presence of OAC^-, whereas stick-like HC_6N_3–CO_2–$Zn(NO_3)_2$ with a size of ~0.98 μm length and ~68 nm width was acquired with the participation of NO_3^- (Fig. 5i and i1). Similarly, a large layer of HC_{10}–N_4–CO_2–$Zn(OAC)_2$ with a thickness of ~100 nm

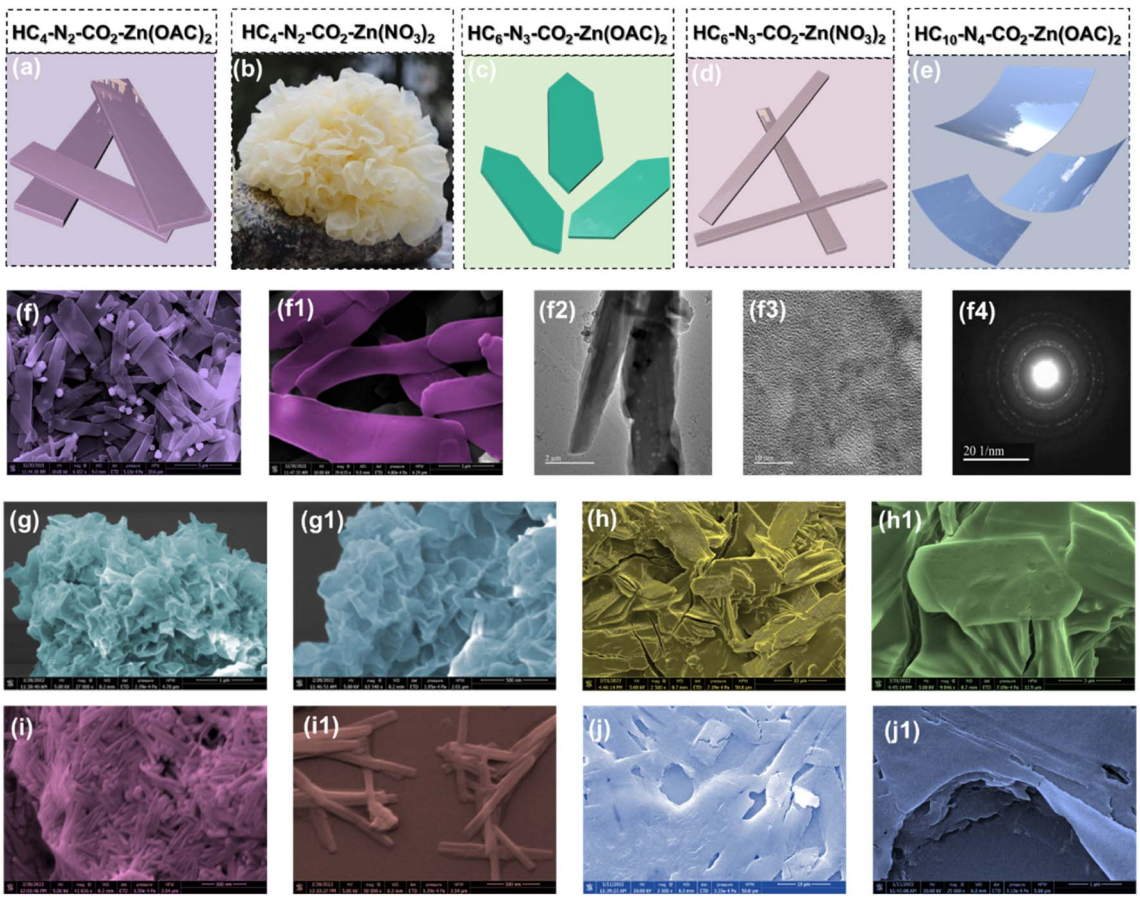

Fig. 5 MOF morphologies analyses. (a–e) Models of different MOF morphologies. (f and f1) FESEM of high aspect ratio laminar HC_4–N_2–CO_2–$Zn(OAC)_2$. (f2 and f3) HR-FETEM image. (f4) SAED pattern of HC_4–N_2–CO_2–$Zn(NO_3)_2$. (g and g1) Tremella-shape HC_4–N_2–CO_2–$Zn(NO_3)_2$. (h and h1) Blocky structure HC_6–N_3–CO_2–$Zn(OAC)_2$. (i and i1) Stick-like HC_6–N_3–CO_2–$Zn(NO_3)_2$. (j and j1) Large layer HC_{10}–N_4–CO_2–$Zn(OAC)_2$. All FESEM images were colored for visual effect.

was acquired from HC_{10}–N_4–CO_2, as demonstrated in Fig. 5j and j1, under heating after the reaction. These results reconfirmed that different anions have a crucial influence on the formation of MOFs.

In addition to the microscopic morphology, the structural characteristics of HC_x–N_y–CO_2–Zn were also analyzed. As shown in Fig. 6a, the XRD pattern indicates that the appearance of new X-ray diffraction peaks at 8.9, 10.2 and 37.9° are attributed to the successful formation of crystals, while the original intrinsic characteristic peaks of HC_4–N_2 are mainly at 15.5, 18.8, 19.9 and 22.5°. The diffraction peak at 10.2° is the dominant peak of MOFs, which is associated with the (220) crystal plane of MOFs.[46] The characteristic X-ray diffraction peaks of HC_4–N_2–CO_2–$ZnSO_4$ are at 13.2, 14.5, 18.1, 20.5 and 30.1°, which are completely different from those of HC_4–N_2–CO_2–$Zn(OAC)_2$, further demonstrating the influence of different anions (SO_4^{2-} and OAC^-) on crystal structures. For HC_6–N_3–CO_2–$Zn(OAC)_2$, the X-ray characteristic diffraction peaks located at 9.9, 11.9, 13.9, 15.2 and 16.9° belong to the crystal structure of the stably existing HC_6–N_3–CO_2–$Zn(OAC)_2$ (Fig. 6b). The diffraction peak at 9.9° is its main peak. Regarding HC_{10}–N_4–CO_2–$Zn(OAC)_2$, the characteristic X-ray diffraction peaks at 8.9, 9.9, 10.8 and 15.8° are attributed to the crystalline structure of HC_{10}–N_4–CO_2–$Zn(OAC)_2$ (Fig. 6c), where the diffraction peak at 10.8° is its dominant peak. In addition, we carried out the BET surface areas and pore size analysis of MOFs. HC_4–N_2–CO_2–$Zn(OAC)_2$, HC_6–N_3–CO_2–$Zn(NO_3)_2$, and HC_{10}–N_4–CO_2–$Zn(OAC)_2$ have specific surface areas of 575, 456, and 127 $m^2\ g^{-1}$, respectively. The pore size of MOF increased with the increase of N heterocycle, which is 0.64 0.78, 1.02 nm, separately (Fig. S13†). The aperture of MOFs is mainly less than 2 nm (micropore), so we choose the CO_2 isotherm. The temperature of the CO_2 isotherm is 195 K. Horvath–Kawazoe (HK) method was used to test the micropores of MOFs.

Thermal stability of HC_x–N_y–CO_2–$Zn(OAC)_2$ MOFs

The formation of functional groups based on carbamate has been widely studied in the field of CO_2 absorption.[47,48] The C–N

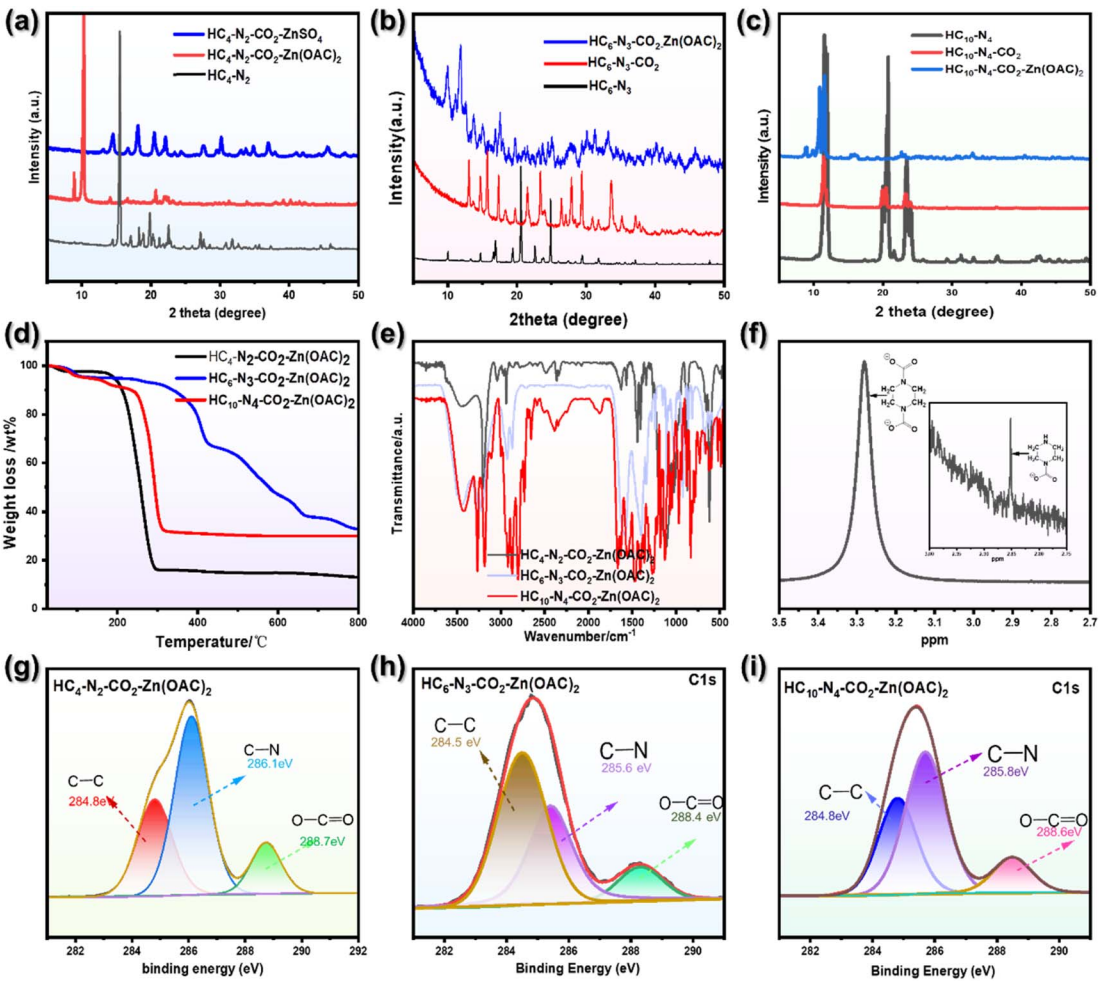

Fig. 6 Property analyses of HC_x–N_y–CO_2–Zn. (a) Comparison of PXRD patterns ($\lambda_{Cu} = 1.5406$ Å) of HC_4–N_2, HC_4–N_2–CO_2–$ZnSO_4$/$Zn(OAC)_2$. (b) HC_6–N_3–CO_2, HC_6–N_3–CO_2–$Zn(OAC)_2$. (c) HC_{10}–N_4, HC_{10}–N_4–CO_2, HC_{10}–N_4–CO_2–$Zn(OAC)_2$. (d) TGA analysis of HC_x–N_y–CO_2–$Zn(OAC)_2$ under N_2 atmosphere. (e) FT-IR characterization of HC_x–N_y–CO_2–$Zn(OAC)_2$. (f) ^1H NMR spectrum of HC_4–N_2–CO_2–$Zn(OAC)_2$. (g–i) The high-resolution XPS spectra of C 1s in HC_4–N_2–CO_2–$Zn(OAC)_2$. (h) HC_6–N_3–CO_2–$Zn(OAC)_2$. (i) HC_{10}–N_4–CO_2–$Zn(OAC)_2$ samples. Property analyses of HC_x–N_y–CO_2–Zn.

bond of carbamate can be formed rapidly and then destroyed immediately at a lower temperature according to a step adsorption model with special characteristics of rapid adsorption and desorption. Therefore, most carbamates are thermodynamically unstable because of weak C–N bonds that result in ready dissociation of carbamate bonds under heating or low pressures.[49] To interrogate the enhanced thermal stability of carbamate-incorporated MOFs, thermal gravimetric analyses (TGA) of HC_x–N_y–CO_2–$Zn(OAC)_2$ were performed for a comparative study (Fig. 6d). The mass of all samples decreased slightly between room temperature and 100 °C, which resulted from the trace organic content (IPA, MeCN) or moisture in the samples. The onset temperatures for the weight loss were 202 °C for HC_4–N_2–CO_2–$Zn(OAC)_2$, 352 °C for HC_6–N_3–CO_2–$Zn(OAC)_2$, and 252 °C for HC_{10}–N_4–CO_2–$Zn(OAC)_2$. Compared with HC_4–N_2–CO_2,[50] the thermal stability of all MOFs was enhanced, and HC_6–N_3–CO_2–$Zn(OAC)_2$ displayed the highest thermal stability in all MOFs.

Chemical component analyses

The Fourier transform infrared spectrum (FT-IR) of HC_x–N_y–CO_2–$Zn(OAC)_2$ exhibits a characteristic peak at 522–535 cm^{-1} (Fig. 6e, S14 and S15†). The peak is in good agreement with the stretching vibration of μ_4-O-Zn of the $[Zn_4O(CO_2)_6]$ clusters,[51] confirming the formation of $Zn_4O(CO_2)_6$. The peak at 2360 cm^{-1} is attributed to carbamate.[52] The infrared peak at 2500–2600 cm^{-1} is derived from the generated quaternary ammonium salt (zwitterion). This indicates that CO_2 is successfully involved in the reaction. To monitor the HC_x–N_y–CO_2 formation from HC_x–N_y, the ^1H NMR spectrum of HC_x–N_y–CO_2–$Zn(OAC)_2$ was acquired (Fig. 6f, S16 and S17†). Fig. 6f depicts two peaks at 3.28 and 2.85 ppm caused by CO_2 absorption in the MOFs, corresponding to mono-carbamate and di-carbamate, respectively.[53,54] Ultimately, the integral of peak area verified that 99.96% of HC_4–N_2 reacted with CO_2 to form HC_4–N_2–CO_2 di-carbamate, only 0.04% of HC_4–N_2 to form mono-carbamate, and no HC_4–N_2 starting material was found, indicating that HC_4–N_2 had high reactivity, which was consistent with the aforementioned experiments (Fig. S7†). However, as far as HC_6–N_3 and HC_{10}–N_4 are concerned, owing to the excessively long reaction path and steric hindrance, few of them form tri-carbamate and tetra-carbamate, while most secondary amine groups react incompletely with CO_2 to form mono-carbamate and di-carbamate or tri-carbamate (Fig. S16 and S17†). In addition, as illustrated in Fig. 6g–i and S18,† XPS analyses further verified the composition of MOFs. By fitting the peaks of the C 1s spectrum, three peaks of binding energies at 288.7, 288.4 and 288.6 eV were assigned to the emerging target group O–C=O of HC_4–N_2–CO_2–$Zn(OAC)_2$, HC_6–N_3–CO_2–$Zn(OAC)_2$ and HC_{10}–N_4–CO_2–$Zn(OAC)_2$, respectively, indicating the successful formation of carbamate.[55,56] The peak areas of O–C=O calculated by integral quantitative analyses corroborated that 37.04%, 28.412%, and 37.02% CO_2 were introduced into the HC_x–N_y–CO_2–$Zn(OAC)_2$ samples, which suggested that ultrahigh levels of CO_2 were utilized to prepare MOFs. Furthermore, fine Zn 2p, N 1s, and O 1s XPS spectra of different MOFs samples were analyzed, which showed similar atomic proportions (Fig. S19†).

Gas separation performance

As an alternative to traditional energy-intensive gas separation approaches, membrane-based gas separation has shown remarkable advantages in terms of low energy consumption, easy operation, eco-friendship, and small footprint. Among various materials, MOFs such as ZIF-8, HZIF-8, UiO-66, and Cu(BDC) have been extensively studied as advanced fillers for constructing functional mixed matrix membranes (MMMs).[57] The MMMs obtained *via* the combination of MOFs and a polymer matrix are one of the most promising solutions for gas separation (Fig. 7a). To evaluate the performance of our obtained MOFs, HC_6–N_3–CO_2–$Zn(NO)_3$, as a filler, was mixed with PIM-1. As an emerging membrane material first developed by Budd *et al.* in 2004,[58] PIM-1 with ladder-like structures (Fig. 7b), contortion sites, irregular and kinked chain architecture, interconnected micropores and high specific surface area exhibit ultrahigh gas permeability. However, inefficient packing of PIM-1 chains leads to a non-equilibrium state where molecular relaxation occurs over time, reaching an equilibrium state and causing the losses of fractional free volume and permeability during the physical aging process.[59] Besides, achieving a desirable match between polymers and MOFs for the development of advanced MMMs is challenging, especially when the emerging highly permeable PIM-1 materials are deployed. New synthetic HC_6–N_3–CO_2–$Zn(NO)_3$ with flexible skeleton and nitrogen-rich characteristics may effectively disrupt PIM-1 chain packing and create additional gas transport channels to improve CO_2 separation performance.

Fig. 7 illustrates the molecular structure of PIM-1, gas separation process, membrane morphology and pore characteristics, as well as separation performance. PIM-1 was synthesized from a polycondensation reaction between 5,5′,6,6′-tetrahydroxy-3,3,3′,3′-tetramethyl-1,1′-spirobisindane (TTSBI) and 1,4-dicyanotetrafluorobenzene (TFTPN). It had a light yellow color and amorphous morphology (Fig. S20†). HC_6–N_3–CO_2–$Zn(NO_3)_2$ was dispersed in a PIM-1 solution with a loading of 1 wt% and then cast as polymer membranes with a thickness of ~50 μm (Fig. 7g and S21†). The resultant MMMs had a smooth top and rough bottom surfaces (Fig. 7e and f, respectively), suggesting that the stick-shaped HC_6–N_3–CO_2–$Zn(NO_3)_2$ piled up from the bottom according to the solidification process for HC_6–N_3–CO_2–$Zn(NO_3)_2$ MMMs (Fig. 7c). This nonaligned, randomly oriented HC_6–N_3–CO_2–$Zn(NO_3)_2$ stick distribution would lead to a selective gas permeation highway to enhance the overall separation performance (Fig. 7d). According to Fig. S22–S24,† the chemical composition of PIM-1 and PIM-1/HC_6–N_3–CO_2–$Zn(NO_3)_2$ (1%) was additionally confirmed by FTIR and XPS analyses. As shown in Fig. S25 and S26,† thermal degradation of HC_6–N_3–CO_2–$Zn(NO_3)_2$ powders and PIM-1 started at around 302 °C and 490 °C, separately. Above this temperature, a continuous weight loss was observed. Thermal stability was improved with the incorporation of HC_6–N_3–CO_2–$Zn(NO_3)_2$ nanoparticles into the PIM-1 matrix because

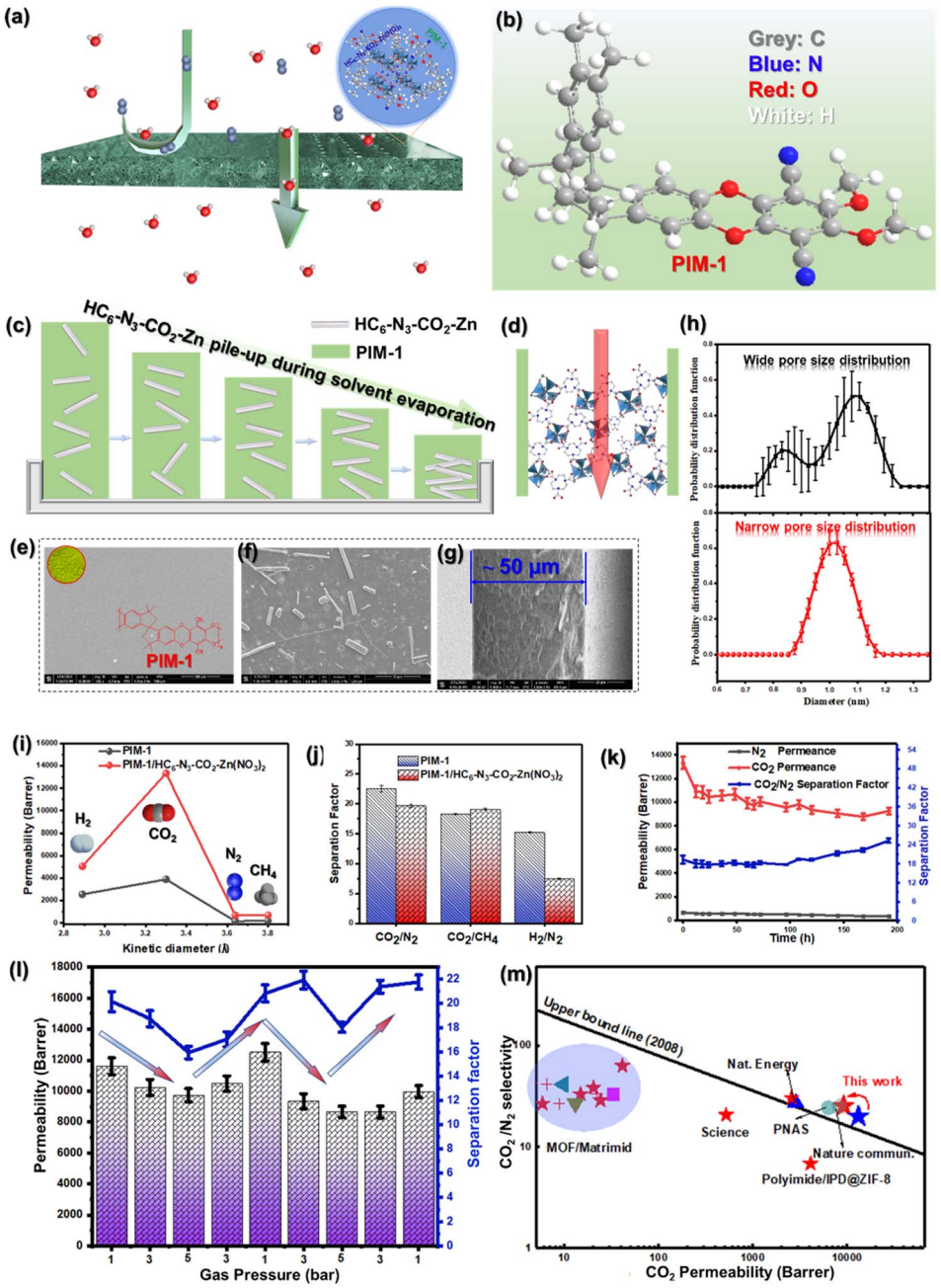

Fig. 7 Mixed matrix membranes for gas separation (a) diagram of gas separation through a membrane. (b) Ladder-like molecular structure of PIM-1 (grey: C, blue: N, red: O, white: H). (c) Illustration of the solidification process of the stick-shaped PIM-1/HC_6–N_3–CO_2–$Zn(NO_3)_2$ (1%) membrane. (d) Schematic illustration of gas transport channels through the PIM-1/HC_6–N_3–CO_2–$Zn(NO_3)_2$ membrane. (e–g) Top view, bottom view and cross-section of the 1 wt% PIM-1/HC_6–N_3–CO_2–$Zn(NO_3)_2$ (1%) membrane. (h) Free volume hole diameters of pure PIM-1 membrane (top) and PIM-1/HC_6–N_3–CO_2–$Zn(NO_3)_2$ (1%) MMMs (bottom) determined by positron annihilation lifetime distributions (PALS) under vacuum at 298 K. (i) Single-gas separation permeability of PIM-1, PIM-1/HC_6–N_3–CO_2–$Zn(NO_3)_2$ (1%) membranes as a function of gas kinetic diameter at 298 K and 2 bar. (j) Separation factors of PIM-1 and 1 wt% PIM-1/HC_6–N_3–CO_2–$Zn(NO_3)_2$ (1%) membranes for CO_2/N_2, CO_2/CH_4 and H_2/N_2 separations. (k) Long-term tests of 1 wt% PIM-1/HC_6–N_3–CO_2–$Zn(NO_3)_2$ (1%) MMMs for CO_2 and N_2 at 298 K and 2 bar. (l) CO_2 permeability and CO_2/N_2 separation factor of 1 wt% PIM-1/HC_6–N_3–CO_2–$Zn(NO_3)_2$ (1%) MMMs as a function of pressure. (m) A comparison of the Robeson upper bound for CO_2/N_2 separation between 1 wt% PIM-1/HC_6–N_3–CO_2–$Zn(NO_3)_2$ (1%) MMMs and literature data. Information on the data points is also given in ESI Table 7.†

the PIM-1/HC_6–N_3–CO_2–$Zn(NO_3)_2$ (1%) MMMs had a high decomposition temperature than that of PIM-1 pure membrane.

PALS is an advanced technology to probe the pore (or free volume) sizes and PSD of membranes. Fig. 7h, S27, S28 and Table S3† show the pore sizes and PSD measured by PALS under

vacuum at 298 K. Consistent with the previous reports,[60,61] the PIM-1 membrane had two pores with diameters of 8.3 Å and 10.9 Å. Interestingly, the PIM-1/HC_6–N_3–CO_2–$Zn(NO_3)_2$ (1%) membrane exhibited a relatively higher intensity for the peak at around 10.1 Å and a narrower PSD than the PIM-1 membrane, possibly due to the effects of hydrogen bonding or coordination between MOFs ligands or metals and PIM-1 skeleton.[62] Overall, the above results confirmed that the introduction of HC_6–N_3–CO_2–$Zn(NO_3)_2$ into PIM-1 could effectively tailor the membrane pore characteristics, which was beneficial to enhance the gas transport, as revealed in the following section.

The gas separation performances were studied using a constant volume-variable pressure method *via* a homemade apparatus, including the gas source, membrane modules, vacuum and detecting system (Fig. S29†). The membranes were wrapped with tape for testing (Fig. S31 and S32†). The gas permeability of membranes decreased in the order of CO_2 (kinetic diameter of 3.30 Å) > H_2 (2.89 Å) > CH_4 (3.76 Å) > N_2 (3.64 Å) (Table S4†). For PIM-1 membranes, the gas permeabilities were 2566 (H_2), 3898 (CO_2), 171 (N_2), 210 (CH_4) barrer, respectively (Fig. 7i), and the ideal selectivity of CO_2/N_2 (CO_2/CH_4) was 22 (18). For the PIM-1/HC_6–N_3–CO_2–$Zn(NO_3)_2$ (1%) MMMs, the gas permeability increased dramatically when HC_6–N_3–CO_2–$Zn(NO_3)_2$ was loaded, while the ideal selectivity was almost unchanged. The CO_2 permeability dramatically increased from 3898 to 13 343 barrer and the CO_2/N_2 and CO_2/CH_4 selectivity changed from 22 to 20 and 18 to 19 (Fig. 7i, j and Table S5†). Further, we collected more data under different HC_6–N_3–CO_2–$Zn(NO_3)_2$ loadings (0.5 wt%, 1.5 wt%, 2.0 wt%). With the increase in MOF contents, CO_2 permeability increased significantly from 5509 (0.5 wt%), 14 377 (1.5 wt%) to 16 377 (2.0 wt%), While the selectivity of CO_2/N_2 decreased significantly from 22.2 (0.5 wt%), 17.8 (1.5 wt%) to 16.3 (2.0 wt%) (Fig. S33†). Therefore, 1.0 wt% HC_6–N_3–CO_2–$Zn(NO_3)_2$ loading MMM had the best performance in terms of selectivity and permeability. The above results indicated that the CO_2 permeability of the MMMs can be significantly increased without much compromise in selectivity, which is conducive to improving the high productivity of the MMMs for practical applications.

Physical aging is a phenomenon where glassy materials relax to a denser configuration with time.[63] Therefore, PIM-1 by itself, with abundant pore volume due to the poor chain packing, can be detrimental to its permeability over extended time periods but gains in selectivity *via* reducing the fractional free volume and pore size from a non-equilibrium state to a more energetically favored state.[64] The addition of HC_6–N_3–CO_2–$Zn(NO_3)_2$ MOFs to PIM-1 was found to stabilize this aging behavior. The partially unreacted HC_6–N_3 on the surface of HC_6–N_3–CO_2–$Zn(NO_3)_2$ sticks interacted with the nitrile groups of PIM-1. It not only formed defect-free matrix-filler interfaces with good compatibility but also potentially restricted chain movements of PIM-1 over time. The permeability of CO_2 decreased slightly from 13 343 to 9264 barrer in 192 h, and the selectivity increased from 20.0 to 25.5 (Fig. 7k and Table S6†). Therefore, PIM-1/HC_6–N_3–CO_2–$Zn(NO_3)_2$ MMMs (1%) have good anti-ageing properties for gas separation.

Since CO_2 would plasticize the membranes at high pressures, it is important to understand the effect of CO_2 pressure on CO_2 permeability and plasticization behavior of PIM-1/HC_6–N_3–CO_2–$Zn(NO_3)_2$ (1%). The separation performance of PIM-1/HC_6–N_3–CO_2–$Zn(NO_3)_2$ (1%) was assessed under various feed pressures. As shown in Fig. 7l, both gas permeability and selectivity slightly decreased with increasing feed pressure. Increasing the feed pressure to 5 bar led to a decrease in CO_2 permeability by ≈16%, and the permeability slightly decreased after restoring the pressure to the initial pressure, indicating that less plasticization was generated in this pressure range. Meanwhile, increasing the pressure to 5 bar led to a decrease in the CO_2/N_2 separation factor by ≈20% (Table S7†). Afterwards, the CO_2 permeability and the CO_2/N_2 selectivity had small changes during pressure cycling, implying that the membrane had good plasticization resistance. Fig. 7m and S34† compare the CO_2/N_2 and CO_2/CH_4 separation performance of PIM-1/HC_6–N_3–CO_2–$Zn(NO_3)_2$ (1%) and other polymer/MOF MMMs in a Robeson's upper-bound plot.[57] As expected, the PIM-1/HC_6–N_3–CO_2–$Zn(NO_3)_2$ (1%) membrane easily surpasses the upper bound and demonstrates significant superiority to various reported polymer/MOFs MMMs (Table S8†). The binary CO_2/N_2 (50/50) mixed-gas performance of PIM-1 and PIM-1/HC_6–N_3–CO_2–$Zn(NO_3)_2$ (1%) membranes with a feed pressure of 2 bar is shown in Fig. 2. All of the membranes provided a lower CO_2 permeability under mixed feeding gas than single gas under the same conditions, which is caused by the competitive sorption mechanism between CO_2 and N_2. N_2 adsorbed in the membranes reduced the CO_2 transport. The CO_2 permeability of PIM-1, PIM-1/HC_6–N_3–CO_2–$Zn(NO_3)_2$ (1%) decreased from 3898, 13 343 barrer using a single feeding of CO_2 to 2039, 7377 barrer with upstream charged with 2 bar CO_2/N_2 (50/50) mixed gas, respectively. The CO_2/N_2 selectivity of the PIM-1, PIM-1/HC_6–N_3–CO_2–$Zn(NO_3)_2$ (1%) membranes decreased from 22 to 19.3 and from 20 to 19.1, separately, after the upstream charged with CO_2/N_2 (50/50) mixed gas as the feeding gas (Fig. S35†).

Conclusion

The nitrogen-rich heterocycles were applied not only for CO_2 capture from the atmosphere but also green utilization for MOFs preparation. For heterocycles HC_x–N_y, the unique merits, such as (i) abundant nucleophilic absorption sites, (ii) high absorption capacity and rate, (iii) symmetrical geometry, and (iv) flexible and variable structure, endow them with a superior DAC capacity. The white precipitates (HC_x–N_y–CO_2) were obtained based on the phase change mechanism when the nucleophilic HC_x–N_y was in contact with electrophilic CO_2. The high CO_2 absorption efficiency of 99% was demonstrated for a long duration of 12 h even under ultralow CO_2 concentration (437 ppm), which shows the practical DAC application. The crystalline carbamate-based MOFs with luxuriant morphologies were prepared from the resultant HC_x–N_y–CO_2 ligands and metal clusters. The incorporation of carbamate-based MOFs into the PIM-1 membrane rearranges the architecture of micropore sizes and pore size distribution, and provides more transport channels for CO_2 separation from flue gas, which

breaks the trade-off limitation between permeability and selectivity, and surpasses the conventional upper bound line. Based on the above work, the novel nitrogen-rich heterocyclic materials show significant promise for direct air carbon capture, high value-added product utilization, high-efficiency CO_2 separation and capture from flue gas, which will accelerate the transition of our world from abundant CO_2 emission to the negative carbon emission and open a boulevard for the future development of CCUS.

Conflicts of interest

There are no conflicts to declare.

Acknowledgements

The authors would like to thank the financial support from the National Key Research and Development Program of China (2022YFB3805200), Shanxi Yanchang Petroleum (Group) Co, Ltd (2022ZKD-04, EF2400000006), Young Talent Programme (GG2400007003, KY2400000020), the National Natural Science Foundation of China (Grant 12275270), the Double First-Class Initiative University of Science and Technology of China (YD2400002003, KY2400000004) and the Fundamental Research Funds for the Central Universities (WK2400000004, KY2400000008). Prof. Chung would also like to thank the Yushan Scholar Program supported by the Ministry of Education, Taiwan. Special thanks are given to Professor Hanqing Yu, Zhouqing Xie, Guoping Sheng, Yang Mu, Xianwei Liu, Wenwei Li, and Jiejie Chen for their valuable assistance and fruitful discussions in the research process. This work was partially carried out at the Instrument Center for Physical Science, University of Science and Technology of China.

References

1 J. S. Sawyer, *Nature*, 1972, **239**, 23–26.
2 J. E. Tierney, C. J. Poulsen, I. P. Montañez, T. Bhattacharya, R. Feng, H. L. Ford, B. Hönisch, G. N. Inglis, S. V. Petersen, N. Sagoo, C. R. Tabor, K. Thirumalai, J. Zhu, N. J. Burls, G. L. Foster, Y. Goddéris, B. T. Huber, L. C. Ivany, S. K. Turner, D. J. Lunt, J. C. McElwain, B. J. W. Mills, B. L. Otto-Bliesner, A. Ridgwell and Y. G. Zhan, *Science*, 2020, **370**, 1–9.
3 S. Pan, Y. Chen, L. Fan, H. Kim, X. Gao, T. Ling, P. C. Chiang, S. Pei and G. Gu, *Nat. Sustain.*, 2020, **3**, 399–405.
4 Z. Liu, Z. Deng, S. J. Davis, C. Giron and P. Ciais, *Nat. Rev. Earth Environ.*, 2022, **3**, 217–219.
5 C. Duffy, R. Prudhomme, B. Duffy, J. Gibbons, P. P. M. Iannetta, C. O'Donoghue, M. Ryan and D. Styles, *Nat. Sustain.*, 2022, **5**, 973–980.
6 M. Roelfsema, H. L. Soest, M. Harmsen, D. P. Vuuren, C. Bertram, *et al.*, *Nat. Commun.*, 2020, **11**, 1–12.
7 S. S. Eloy, R. M. Christopher, A. D. Stephanie and W. J. Christopher, *Chem. Rev.*, 2016, **116**, 11840–11876.
8 K. S. Lackner, H. Ziock and P. Grimes, Carbon dioxide extraction from air: is it an option?, in *proceedings of the 24th annual technical conference on coal utilization & fuel systems; clearwater*, United States, 1999, N. p., 02.
9 Y. H. Wang, J. Y. Zhao, S. Zhang, Z. M. Zhang, Z. T. Zhu, M. D. Wang, B. H. Lyu, G. W. He, F. S. Pan and Z. Y. Jiang, *Mater. Horiz.*, 2023, **10**, 5016–5021.
10 J. B. Lin, T. T. T. Nguyen, R. Vaidhyanathan, J. Burner, J. M. Taylor, H. Durekova, F. Akhtar, R. K. Mah, O. Ghaffari-Nik, S. Marx, N. Fylstra1, S. S. Iremonger, K. W. Dawson1, P. Sarkar, P. Hovington, A. Rajendran, T. K. Woo and G. K. H. Shimizu, *Science*, 2021, **374**, 1464–1469.
11 E. J. Kim, R. L. Siegelman, H. Jiang, A. C. Forse, J. H. Lee, J. D. Martell, P. J. Milner, J. M. Falkowski, J. B. Neaton, J. A. Reimer, S. C. Weston and J. R. Long, *Science*, 2020, **369**, 392.
12 Y. Li, X. Lu, S. Xi, D. Luan, X. Wang and X. Lou, *Angew. Chem., Int. Ed.*, 2022, **61**, e202201491.
13 Z. Florjanczyk, G. Rokicki, P. G. Parzuchowski, M. Mazurek-Budzynska and M. Debowski, Polymeric Materials Based on Carbon Dioxide: A Brief Review of Studies Carried Out at the Faculty of Chemistry, Warsaw University of Technology, *Polymers*, 2022, **14**, 718.
14 T. Cai, H. Sun, J. Qiao, L. Zhu, F. Zhang, J. Zhang, Z. Tang, X. Wei, J. Yang, Q. Yuan, W. Wang, X. Yang, H. Chu, Q. Wang, C. You, H. Ma, Y. Sun, Y. Li, C. Li, H. Jiang, Q. Wang and Y. Ma, *Science*, 2021, **37**, 1523–1527.
15 T. Zheng, M. Zhang, L. Wu, S. Guo, X. Liu, J. Zhao, W. Xue, J. Li, C. Liu, X. Li, Q. Jiang, J. Bao, J. Zeng, T. Yu and C. Xia, *Nat. Catal.*, 2022, **5**, 388.
16 Z. Yin, S. Wan, J. Yang, M. Kurmoo and M. H. Zeng, *Coord. Chem. Rev.*, 2019, **378**, 500–512.
17 G. Cai, P. Yan, L. Zhang, H. Zhou and H. Jiang, *Chem. Rev.*, 2021, **121**, 12278–12326.
18 J. Canivet, A. Fateeva, Y. Guo, B. Coasnecd and D. Farrusseng, *Chem. Soc. Rev.*, 2014, **43**, 5594.
19 Z. Han, J. Li, W. Lu, K. Wang, Y. Chen, X. Zhang, L. Lin, X. Han, S. J. Teat, M. D. Frogley, S. Yang, W. Shi and P. Cheng, *Angew. Chem., Int. Ed.*, 2022, **134**, e202115585.
20 R. Wei, X. Liu, Z. Zhou, C. Chen, Y. Yuan, Z. Li, X. Li, X. Dong, D. Lu, Y. Han and Z. Lai, *Sci. Adv.*, 2022, **8**, eabm6741.
21 H. Li, S. Zhao, S. Zang and J. Li, *Chem. Soc. Rev.*, 2020, **49**, 6364–6401.
22 Z. Xue, D. Luan, H. Zhang and X. Lou, *Joule*, 2022, **6**, 92–133.
23 P. Horcajada, T. Chalati, C. Serre, B. Gillet, C. Sebrie, T. Baati, J. F. Eubank, D. Heurtaux, P. Clayette, C. Kreuz, J. Chang, Y. K. Hwang, V. Marsaud, P. N. Bories, L. Cynober, S. Gil, G. Férey, P. Couvreur and R. Gref, *Nat. Mater.*, 2010, **9**, 172–178.
24 N. Huang, K. Wang, H. Drake, P. Cai, J. Pang, J. Li, S. Che, L. Huang, Q. Wang and H. Zhou, *J. Am. Chem. Soc.*, 2018, **140**, 6383–6390.
25 S. H. Jhung, J. H. Lee, J. W. Yoon, C. Serre, G. Férey and J. Chang, *Adv. Mater.*, 2007, **19**, 121–124.
26 R. Abazari, A. R. Mahjoub and G. Salehi, *J. Hazard. Mater.*, 2019, **365**, 921–931.
27 A. Stolle, T. Szuppa, S. E. S. Leonhardta and B. Ondruschka, *Chem. Soc. Rev.*, 2011, **40**, 2317.

28 K. Kadota, Y. L. Hong, Y. Nishiyama, E. Sivaniah, D. Packwood and S. Horike, *J. Am. Chem. Soc.*, 2021, **143**, 16750–16757.
29 S. Wang, N. Xhaferaj, M. Wahiduzzaman, K. Oyekan, X. Li, K. Wei, B. Zheng, A. Tissot, J. Marrot, W. Shepard, C. Martineau-Corcos, Y. Filinchuk, K. Tan, G. Maurin and C. Serre, *J. Am. Chem. Soc.*, 2019, **141**, 17207–17216.
30 E. K. Young, H. C. Jeong, C. N. Sung and I. Y. Yeo, *Ind. Eng. Chem. Res.*, 2011, **50**, 9306–9313.
31 H. Mao, J. Tang, G. S. Day, Y. Peng, H. Wang, X. Xiao, Y. Yang, Y. Jiang, S. Chen, D. M. Halat, A. Lund, X. Lv, W. Zhang, C. Yang, Z. Lin, H. Zhou, A. Pines, Y. Cui and J. A. Reimer, *Sci. Adv.*, 2022, **8**, eabo6849.
32 K. Suresh, D. Aulakh, J. Purewal, D. J. Siegel, M. Veenstra and A. J. Matzger, *J. Am. Chem. Soc.*, 2021, **143**, 10727–10734.
33 A. Majumder, S. Shit, C. R. Choudhury, S. R. Batten, G. Pilet, D. Luneau, N. Daro, J. P. Sutter, N. Chattopadhyay and S. Mitra, *Inorg. Chim. Acta*, 2005, **35**, 3855–3864.
34 J. Hu, X. Yao, M. Zhang, L. Qin, Y. Li, Z. Guo, H. Zheng and Z. Xue, *Cryst. Growth Des.*, 2012, **12**, 3426–3435.
35 H. Chao, Z. Zhou, W. He, M. Li, X. Yuan, P. Su, J. Song and Y. Yang, *ACS Appl. Mater. Interfaces*, 2022, **14**, 20641–20651.
36 S. Kandambeth, V. Venkatesh, D. B. Shinde, S. Kumari, A. Halder, S. Verma and R. Banerjee, *Nat. Commun.*, 2015, **6**, 1–10.
37 Q. Dang, H. Huang, L. Li, X. L. Lyu, S. Zhong, Y. Yu and D. Xu, *Chem. Mater.*, 2021, **33**, 5690–5699.
38 X. Yang, Y. Zhu, D. Wu, M. Li, Y. He, L. Huang and M. Gu, *Adv. Funct. Mater.*, 2022, **32**, 2111391.
39 Y. Li, S. Zhang, W. Cheng, Y. Chen, D. Luan, S. Gao and X. Lou, *Adv. Mater.*, 2022, **34**, 2105204.
40 L. B. Vilhelmsen, K. S. Walton and D. S. Sholl, *J. Am. Chem. Soc.*, 2012, **134**, 12807–12816.
41 C. Wang, D. Liu, Z. Xie and W. Lin, *Inorg. Chem.*, 2014, **53**, 1331–1338.
42 P. J. Beldon, L. Fábián, R. S. Stein, A. Thirumurugan, A. K. Cheetham and T. Friščić, *Angew. Chem., Int. Ed.*, 2010, **122**, 9834–9837.
43 R. Vilar, *Eur. J. Inorg. Chem.*, 2008, 357–367.
44 T. Friscic, D. G. Reid, I. Halasz, R. S. Stein, R. E. Dinnebier and M. J. Duer, *Angew. Chem., Int. Ed.*, 2010, **49**, 712–715.
45 D. J. Tranchemontagne, J. R. Hunt and O. M. Yaghi, *Tetrahedron*, 2008, **64**, 8553–8557.
46 V. Y. Mao, P. J. Milner, J. H. Lee, A. C. Forse, E. J. Kim, R. L. Siegelman, C. M. McGuirk, L. B. Zasada, J. B. Neaton, J. A. Reimer and J. R. Long, *Angew. Chem., Int. Ed.*, 2020, **59**, 19468–19477.
47 J. D. Martell, L. B. Zasada, A. C. Forse, R. L. Siegelman, M. I. Gonzalez, J. Oktawiec, T. Runcevski, J. Xu, M. Srebro-Hooper, P. J. Milner, K. A. Colwell, J. Autschbach, J. A. Reimer and J. R. Long, *J. Am. Chem. Soc.*, 2017, **139**, 16000–16012.
48 D. J. Heldebrant, P. K. Koech, V. A. Glezakou, R. Rousseau, D. Malhotra and D. C. Cantu, *Chem. Rev.*, 2017, **117**, 9594–9624.
49 K. Kadota, Y. Hong, Y. Nishiyama, E. Sivaniah, D. Packwood and S. Horike, *J. Am. Chem. Soc.*, 2021, **143**, 16750–16757.
50 Y. Wu, H. Pang, W. Yao, X. Wang, S. Yu, Z. Yu and X. Wang, *Sci. Bull.*, 2018, **63**, 831–839.
51 V. A. Gal'perin and A. I. Finkel'shtein, *J. Appl. Spectrosc.*, 1972, **17**, 1176–1178.
52 Y. E. Kim, J. H. Choi, S. C. Nam and Y. I. Yoon, *Ind. Eng. Chem. Res.*, 2011, **50**, 9306–9931.
53 J. T. Cullinane and G. T. Rochelle, *Fluid Ph. Equilib.*, 2005, **227**, 197–213.
54 Y. S. Yu, X. Jiang, Y. W. Fang, J. Y. Chen, J. Kang, Y. Cao and M. Xiang, *Polymers*, 2019, **11**, 1988.
55 J. C. Lv, Q. Q. Zhou, T. Zhi, D. W. Gao and C. X. Wang, *J. Cleaner Prod.*, 2016, **118**, 187e196.
56 Q. H. Qian, P. A. Asinger, M. J. Lee, G. Han, K. M. Rodriguez, S. Lin, F. M. Benedetti, A. X. Wu, W. S. Chi and Z. P. Smith, *Chem. Rev.*, 2020, **120**, 8161–8266.
57 P. M. Budd, E. S. Elabas, B. S. Ghanem, S. Makhseed, N. B. McKeown, K. J. Msayib, C. E. Tattershall and D. Wang, *Adv. Mater.*, 2004, **16**, 456–459.
58 P. M. Budd, E. S. Elabas, B. S. Ghanem, S. Makhseed, N. B. McKeown, K. J. Msayib, C. E. Tattershall and D. Wang, *Adv. Mater.*, 2004, **16**, 456–459.
59 K. M. Rodriguez, S. Lin, A. Wu, X. Han, J. J. Teesdale, C. M. Doherty and Z. P. Smith, *Angew. Chem., Int. Ed.*, 2021, **60**, 6593–6599.
60 C. Geng, Y. Sun, Z. Zhang, Z. Qiao and C. Zhong, *AIChE J.*, 2023, **69**, e18025.
61 Y. Ren, B. Chong, W. Xu, Z. Zhang, L. Liu, Y. Wu, Y. Liu, H. Jiang, X. Liang, H. Wu, H. Zhang, B. Ye, C. Zhong, G. He and Z. Jiang, *Innovation*, 2022, **3**, 100334.
62 C. H. Lau, P. T. Nguyen, M. R. Hill, A. W. Thornton, K. Konstas, C. M. Doherty, R. J. Mulder, L. Bourgeois, A. C. Y. Liu, D. J. Sprouster, J. P. Sullivan, T. J. Bastow, A. J. Hill, D. L. Gin and R. D. Noble, *Angew. Chem., Int. Ed.*, 2014, **53**, 5322–5326.
63 M. Tamaddondar, A. B. Foster, M. Carta, P. Gorgojo, N. B. McKeown and P. M. Budd, *ACS Appl. Mater. Interfaces*, 2020, **12**, 46756–46766.
64 L. M. Robeson, The upper bound revisited, *J. Membr. Sci.*, 2008, **320**, 390–400.